Copyright © 2010 Tech Science Press CMES, vol.62, no.2, pp.113-149, 2010

Meshless Local Petrov-Galerkin Simulation of Buoyancy-Driven Fluid Flow and Heat Transfer in a Cavity with Wavy Side Walls

A. Arefmanesh[1], **M. Najafi**[2] **and M. Nikfar**[3]

Abstract: As some new applications of the meshless local Petrov-Galerkin method (MLPG) with unity as the test function, a number of buoyancy-driven fluid flow natural convection heat transfer problems in cavities with differentially-heated wavy side walls were analyzed. Cavities with a single wavy wall on one side as well as two wavy walls erected on both sides were considered. For the cases of the double wavy walls, two different configurations in terms of the two walls facing each other on the two sides of the cavities symmetrically or non-symmetrically were investigated. All the simulations performed in this work were based on the stream function-vorticity formulation. The work of this study is focused on the cavities filled with incompressible and laminar flow of air with a Prandtl number of 0.71. The moving least-squares interpolations of the field variables were employed in these MLPG numerical calculations. Appropriate parametric and characteristic studies were carried out on all the wavy wall-cavities considered. The analysis focused on the effects of the dimensionless amplitudes, wall's number of undulations, and different Rayleigh numbers on the fluid flow and natural convection heat transfer within the considered enclosures. The results of the MLPG-new applications show smooth Nusselt number distributions and the occurrences of the distributions maxima and minima in the close proximity of the crests and troughs, respectively, as they were supposed to. The logical behavior of the streamlines and the isotherms affected by the appropriate parameters and geometrical characters prove the total validity and feasibility of the code for the new considered applications.

Keywords: meshless, Petrov-Galerkin, buoyancy-driven, cavity, wavy wall

---

[1] Mechanical Engineering Faculty, University of Kashan, Kashan, Iran

[2] Mechanical Engineering Faculty, Islamic Azad University, Science & Research Branch, Tehran, Iran

[3] Mechanical Engineering Graduate Student, University of Kashan, Kashan, Iran

Nomenclature

A	wall amplitude	Ra	Rayleigh number
g	gravitational acceleration	Re	Reynolds number
Gr	Grashof number	S	collection of nodal points
H	cavity height	s-t	streamline coordinates
h	control volume size	T	temperature
L	cavity width	U_{max}	maximum horizontal velocity at vertical centerline
N	MLS interpolation function	V_{max}	maximum vertical velocity at horizontal centerline
n	control volume normal vector	u, v	velocity components
n_A	number of undulations	U, V	dimensionless velocity components
n_k	interpolating node	$\mathbf{x}$	Cartesian coordinates vector
Nu	Nusselt number	x-y	Cartesian coordinates
$\mathbf{P}$	basis vector	X-Y	dimensionless Cartesian coordinates
p	pressure	W	test function
Pr	Prandtl number		

Greek Symbols

α	thermal diffusivity	ρ	density
$\boldsymbol{\alpha}, \boldsymbol{\beta}, \boldsymbol{\gamma}$	unknown coefficients vectors	Ω	dimensionless vorticity, domain
β	thermal expansion coefficient	Ω_I	control volume
φ	weighting function	ω	vorticity
Γ	boundary	Ψ	dimensionless stream function
Γ_h, Γ_I	boundary segment	ψ	stream function
ν	kinematic viscosity	θ	dimensionless temperature

Subscripts

avg	average	*in*	inside
c	cold	*max*	maximum
h	hot	*min*	minimum
I	point or control volume number	*w*	wall

Superscripts

T	transposed	$-$	approximation function
^	nodal value, unit vector	~	vector

1 Introduction

A number of meshless techniques have been proposed in recent years [Atluri and Shen (2002); Atluri (2004)] as some strategies to alleviate the difficulties associated with the mesh generations, relaxing constrains, and interpolations involved in the conventional finite difference or finite volume methods. The diffuse element method proposed by Nayroles, Touzot and Villon [1992] is among the earlier mesh-free techniques. In this method, a collection of nodes and a boundary description are to be adequate to obtain the Galerkin equations. However, an auxiliary grid is still required to evaluate the integrals resulting from applying the Galerkin method to the differential equations. Subsequently, through introducing a regular cell structure as the auxiliary grid, Belytschko, Krongauz, Organ, Flemming and Krysl [1996], and Lu, Belytschko and Gu [1994] transformed the above technique to what is known as the element-free Galerkin method. Zhu and Atluri [1998] introduced a modified collocation method using the actual nodal values of the trial function, as well as, a penalty formulation to enforce the essential boundary conditions in the element-free Galerkin method. The numerical examples solved by them showed that the proposed penalty method did not exhibit any volumetric locking, and retained high rates of convergence for both displacements and strain energy.

In recent years, two other meshless techniques- the meshless local boundary equation method, and the meshless local Petrov-Galerkin (MLPG) method - have been proposed by Zhu, Zhang and Atluri [1998], and Atluri and Zhu [1998, 2000], respectively. To obtain the discretized equations in the above schemes, the shape functions from the moving least-squares (MLS) interpolations are employed in a local weak form of the differential equations over a local sub-domain. Atluri and Zhu [1998] employed the newly developed MLPG method to solve the Laplace and the Poisson's equations, as well as, the potential flow around a cylinder. In another study in the same year, Atluri and Zhu [1998] extended the MLPG method to solve nonlinear boundary value problems. They emphasized in these papers that, compared to the finite element method, the MLPG method was considerably more accurate for computing the values of the unknown variables and their derivatives. Moreover, they pointed out that absolutely no elements were required in the MLPG formulation, and no smoothing technique was required to compute the derivatives. They also showed that the method possessed high rates of convergence with mesh refinement for the Sobolev norms. Atluri's book [2004] presents a recent comprehensive review of the MLPG methods with emphasis on the solid mechanics applications.

In very recent years, substantial research also devoted to the solid mechanics applications of the MLPG method were appeared in the literature. Among them, one can mention the works by Sellountos, Vavourakis and Polyzos [2005]; Sladek J; Sladek V; Wen and Aliabadi [2006]; Han, Liu, Rajendran and Atluri [2006], and Sladek J., Sladek V., Zhang, Solek and Starek [2007]. In addition, in the past few years, some studies devoted to the fluid flow and heat transfer applications of the meshless techniques have been performed. The MLPG method which was applied to the solutions of the convection-diffusion and the Navier-Stokes (N-S) equations by Lin and Atluri [2000, 2001] belongs to this category. In this study, the local weak forms were modified to overcome the so-called Babuska-Brezzi conditions while solving the primitive-variables form of the N-S equations. This work also presented different upwinding schemes in order to obtain stabilized solutions under high Peclet and Reynolds numbers. In another study, Sladek J., Sladek V., and Atluri [2004] employed the MLPG method with the Heaviside step function and the MLS interpolations to analyze the steady as well as the transient heat conductions in a continuously non-homogenous anisotropic medium. Arefmanesh, Najafi and Abdi [2005] applied a variation of the MLPG method with unity as the test function to the convection-diffusion and the potential flow equations.

As far as applications of the MLPG method on the heat conduction analysis, one may mention a few recent studies. Among them, WU, SHEN, and TAO [2007] applied the MLPG collocation method to compute two-dimensional heat conduction problems in an irregular domain. A case which had analytical solution showed that the MLPG method can obtain the desired accuracy. Sladek J, Sladek V, Tan and Atluri [2008] applied the MLPG approach to solve the steady as well as the transient three-dimensional heat conduction problems in a continuously non-homogeneous anisotropic medium. The Laplace transform was used to treat the time dependence of the variables for the transient problems. The meshless approximation based on the MLS method was employed for the implementation. Several examples were presented to demonstrate the veracity and the effectiveness of the numerical approach.

In recent years many different meshless techniques were developed, and were applied on fluid flow and heat transfer problems. A mesh-free approach named local radial basis function-based differential quadrature (RBF-DQ) method was proposed by Shu, Ding, and Yeo [2005] and applied to incompressible flows in the steady and unsteady two-dimensional cases, namely, driven-cavity flow, flow past one isolated cylinder, and flow around two staggered circular cylinders. Excellent numerical results were reported for these cases. Shan, Shu and Lu [2008] used a mesh-free approach called local multiquadric-based differential quadrature (MQ-DQ) method to simulate fluid flow problems with curved boundary in a three-dimensional space. Flow past sphere with various Reynolds numbers was chosen as a test case. The computed solution was compared well with the available data in the literature. A mesh-free Local Radial Basis Function collection method (LRBFCM) was applied in solving an incompressible turbulent flow by Vertnik and Sarler [2009]. The turbulent flow equations were described by the low-Re numbers K-ε model with Jones and launder closure coefficients. The solution was compared with the analytical solution and the solutions through some commercial codes, and reasonably good agreement among the solutions were achieved.

Apart from the above mentioned mesh-free approaches, there are also some numerical convection heat transfer related studies available in the literature. Nicolas, Bermudes, and Baez [2009] investigated the effects of the Rayleigh number and the aspect ratio on the two-dimensional natural convection flows numerically. Ho-Minh, Mai-Duy and Tran-Cong [2009] introduced a Galerkin-radial basis function approached based on the stream function-vorticity formulation to simulate natural convection heat transfer in two-dimensional domains. Using the method, they obtained convergent solution for the problem in a square slot for the Rayleigh numbers up to 10^8. Avila and Solorio [2009] used the spectral element method to simulate two-dimensional convection in a concentric annulus with solid-melting phase-change.

Among more recent studies on the fluid flow and heat transfer applications of the MLPG method is the work of Ching and Chen [2006] in which they used the method to conduct thermo-mechanical analysis on the functionally graded composites under laser heating. Liu [2006] employed the MLPG approach which it was based on the discrete-ordinate equations to solve a radiation heat transfer problem in a multi-dimensional absorbing-emitting-scattering graded index medium. His results showed that the MLPG method used was quite accurate for solving the radiation heat transfer problems. Sladek J., Sladek V., Hellmich, and Eberhardsteiner [2007] applied the MLPG method to solve heat conduction problems in some three-dimensional axisymmetric as well as anisotropic bodies. Very recently, Arefmanesh, Najafi and Abdi [2008] used a variation of the MLPG method with a unity test function to solve a number of non-isothermal fluid flow problems. They employed the stream function-vorticity formulation to solve different test cases, such as, a non-isothermal lid-driven cavity flow with an inlet and an outlet problem. Xue-Hong and Wen-Quan [2008] have applied the MLPG method to solve the steady-state heat conduction in irregular complex domains. They employed the MLS interpolations, and enforced the essential boundary conditions by the transformation method. Their results show that the MLPG method is quite effective for solving heat conduction problems in domains having complex shapes. In another study, Haji Mohammadi [2008] has applied the MLPG method to the incompressible viscous fluid flow. He formulated his considered cases in terms of the stream function-vorticity, and employed the radial basis function interpolations in his approach. Through introducing a new upwinding scheme, he obtained stabilized solutions for the lid-driven cavity flow for Reynolds numbers up to 10^4. Avila and Perez [2008] applied the MLPG approach coupled with a fully implicit velocity-pressure correction algorithm to solve the two-dimensional, steady state incompressible fluid flow equations. The weak forms of these equations were integrated in a local standard domain by the Gauss- Lobatto-Legendre quadrature rule. The Moving Least Square (MLS) scheme was used to generate the interpolation shape functions. In this study, it was concluded that the MLPG method coupled with the implicit procedure used was a reliable methodology to solve the Navier-

Stokes equations. Dehghan and Mirzaei [2009] have used the MLPG method for the unsteady magnetohydrodynamic flow through a pipe of rectangular cross section. They approximated the field variables by the MLS scheme, and employed unity as the test function in the local weak form. They concluded that the employed MLPG method is quite efficient and more flexible compared to the boundary element method. Ma [2005] extended the MLPG method to simulate nonlinear water waves. He, in this work, employed the Heaviside step function as the test function to formulate the weak form over some local sub-domains, acquiring an expression in terms of pressure gradient. The method was validated by simulating various water waves generated by a wavemaker and by motions of a tank. Good agreements of the results with those from the literature were achieved. Ma [2007] used a meshless method called Meshless Local Petrov-Galerkin based on the Rankine source (MLPG-R) and a mesh-based method called Quasi Arbitrary Lagragian-Eulerian Finite Element Method (QALE-FEM) to simulate freak waves. Comparisons were made among the results of the two methods and those from the experiments available in the literature, and good agreements were achieved.

Buoyancy-driven fluid flow and heat transfer in rectangular enclosures with differentially-heated side walls have important industrial applications, such as, design of heat exchangers, solar collectors, and cooling of nuclear reactors to mention a few. Shi and Khodadadi [2003] studied the laminar natural convection heat transfer in a differentially-heated square cavity having a hot thin fin on the hot wall for Rayleigh numbers between 10^4 and 10^7. The effects of the fin's length and its position on the rate of heat transfer were investigated in their work, and a correlation was proposed for the mean Nusselt number in terms of the Rayleigh number, the fin's length, and its position. Laminar natural convection in an inclined, square cavity with a hot wavy wall was studied numerically by Adjlout, Imine, Azzi and Belkadi [2002] using the finite difference method, and the stream function-vorticity formulation. They performed the simulation for different inclination angles, different amplitudes, and different Rayleigh numbers (between 10^4 and 10^6). In their study, two geometrical configurations of a wavy hot wall, called one and three undulations were considered. Their results show that the undulations numbers affect the fluid flow and heat transfer in the considered cavities, resulting in a decrease of the average Nusselt number compared to those of the square cavities. Wang and Chen [2002] employed the finite difference technique to study the non-isothermal flow in a sinusoidally curved converging –diverging channel based on the stream function-vorticity formulation. In their work, they investigated the effects of the wavy geometries, Reynolds, and Prandtl numbers on the flow and heat transfer rates. They concluded that for large amplitude-wavelength ratios, the local Nusselt number increased significantly in the converging section of the wavy-wall channel, while showing a small change in the diverging section. Hence, under such circumstances, the corrugated channel was concluded to be an effective heat transfer device. Natural convection in a wavy enclosure was studied by Das and Mahmud [2003] using the finite volume method. The top and the bottom walls of the enclosure were wavy, and were kept isothermal; while, its side walls were assumed to be straight and adiabatic. Their results showed that the amplitude to wavelength ratio had a significant effect on the average Nusselt number only at low Grashof numbers, but for high Grashof numbers the effect was very small. Sabeur-Bendehina, Adjlout and Imine [2006], in a more recent study, used the finite volume method to investigate the effects of the sinusoidal temperature distribution of the side-walls on the laminar natural convection in a cavity with a hot wavy wall. The top and the bottom walls of the cavity were insulated. They considered two different geometries of the hot wavy wall, called one and three undulations. The results showed that the mean Nusselt number decreased compared to that of the rectangular cavity.

The penalty finite element method was used to solve a two-dimensional, steady and laminar viscous incompressible flow in a sinusoidal corrugated inclined enclosure [Saha; S., Sultana; T., Saha; G., Rahman; M.M. (2008)]. The analysis focused on the natural convection heat transfer for a cavity having two side walls with single corrugation frequency and the corrugation amplitude. The two side walls were kept at a constant temperature, and a constant heat flux source was discretely embedded at the bottom wall. The remaining parts of the bottom surface and the upper wall were considered to be adiabatic, and air was taken to be the working fluid. The study concluded that the average Nusselt numbers increased as the inclination angle increased for different heat source sizes.

Very recently, Al-Amiri, Khanafer, Bull and Pop [2007] investigated the effects of a sinusoidal wavy bottom surface on the mixed convection heat transfer in a lid-driven cavity. The vertical walls of the cavity were insulated while the bottom wavy wall was kept at a uniform temperature higher than that of the top wall. The Galerkin finite element method was employed to solve the governing equations. They considered the effects of the Richardson number, the number of undulations, and the amplitude of the wavy surface on the flow and heat transfer rates in the cavity. They concluded that the average Nusselt number increased with an increase in both the amplitude of the wavy surface and the Reynolds number. They also concluded that for low Richardson numbers, the optimum heat transfer was achieved for a wavy surface having two undulations.

There are very few studies on the applications of the mesh-free methods in the field of natural convection. Sadat and Couturier [2000] used a meshless technique called the diffuse approximation method (DAM) to simulate the laminar buoyancy-driven heat transfer in a square cavity. In another study, Sophy, Sadat, and Prax

[2002] employed the DAM to study the natural convection in a three-dimensional, differentially-heated cubic cavity. As they pointed out, their study was exploratory and needed further investigations to explore the limitations of their formulation fully. Liu [2003] investigated the performance of the MLPG method for simulating the buoyancy-driven heat transfer in a differentially-heated square cavity filled with air for Rayleigh numbers up to 10^5. His results show that the MLPG method is more accurate than the finite difference method using the same uniform nodal distributions.

It seems that emphasis on the applications of the MLPG method on the natural convection for irregular and complex domains are very little in the literature. On this ground, in this work, the MLPG method is extended to focus on the natural convection analysis for cavities with differentially-heated wavy side walls. The simulations performed here are for incompressible, and laminar flow of air in the cavities using the stream function-vorticity formulation. A unity test function, together with the MLS interpolations of the field variables are employed in the numerical calculations. A parametric study is performed, and the effects of the relevant dimensionless groups, such as, the Rayleigh number, the number of undulations, and the dimensionless amplitudes of the wavy walls on the Nusselt number distributions are investigated.

2 Problem Formulation

In this study, a buoyancy-driven flow enclosed within a square cavity having two wavy walls on the two sides is considered. The flow of the fluid and its heat transfer within the cavity are analyzed numerically using the MLPG method with unity as the test function. As depicted schematically in Fig. 1, the height and the width of the cavity are H and L, respectively, with H = L = 1. The length of the cavity perpendicular to the plane of the figure is long enough for the problem to be assumed two-dimensional. The wavy left and right walls of the enclosure are maintained at the constant temperatures of T_h and T_c, respectively, with $T_h > T_c$. The top and bottom walls are insulated, and the cavity is filled with air (Pr = 0.71). The air adjacent to the left wall of the cavity is heated by the wall and expands as it moves upwards, while in the downflowing branch of the cycle, the air is cooled by the right wall as it reaches the bottom of the cavity, developing a clockwise vortex type fluid flow within the cavity.

The appropriate steady-state continuity, momentum, and energy equations are considered. In doing so the y-component of the momentum equation is incorporated with the appropriate natural convection term by employing the Bousinesq approxi-

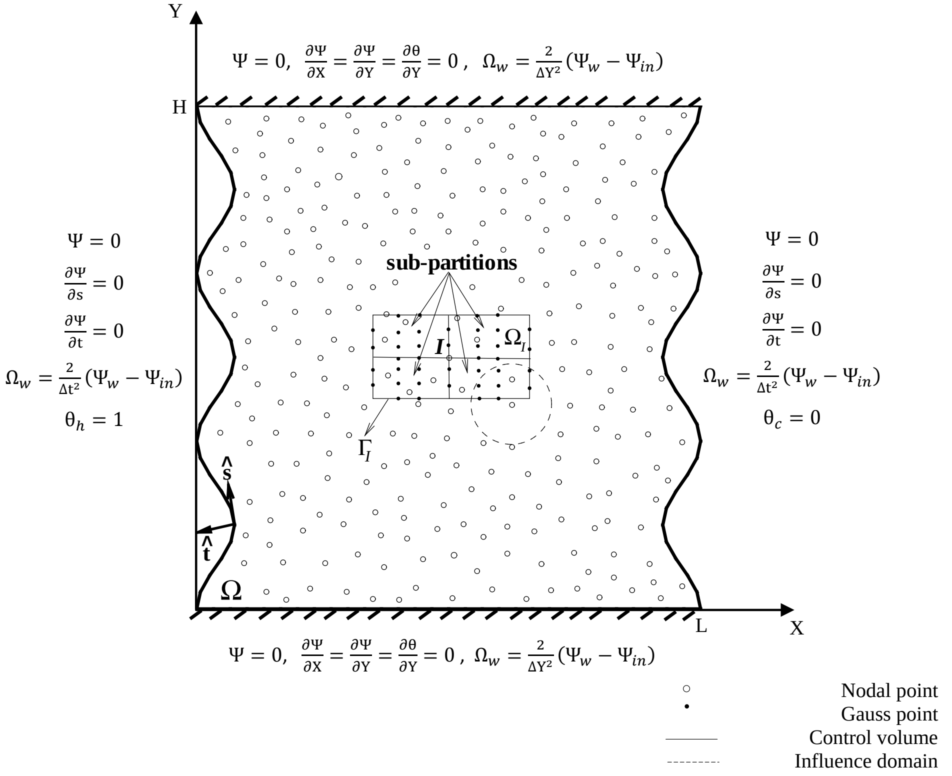

Figure 1: Domain, boundary conditions, and a typical control volume for the buoyancy-driven heat transfer in a cavity with wavy side walls

mation for the incompressible laminar fluid flow within the cavity as follow:

$$\frac{\partial u}{\partial x} + \frac{\partial v}{\partial y} = 0 \tag{1}$$

$$u\frac{\partial u}{\partial x} + v\frac{\partial u}{\partial y} = -\frac{1}{\rho}\frac{\partial p}{\partial x} + \mathscr{V}\left(\frac{\partial^2 u}{\partial x^2} + \frac{\partial^2 u}{\partial y^2}\right), \tag{2a}$$

$$u\frac{\partial v}{\partial x} + v\frac{\partial v}{\partial y} = -\frac{1}{\rho}\frac{\partial p}{\partial y} + \mathscr{V}\left(\frac{\partial^2 v}{\partial x^2} + \frac{\partial^2 v}{\partial y^2}\right) - g\left[1 - \beta\left(T - T_0\right)\right] \tag{2b}$$

$$u\frac{\partial T}{\partial x} + v\frac{\partial T}{\partial y} = \alpha\left(\frac{\partial^2 T}{\partial x^2} + \frac{\partial^2 T}{\partial y^2}\right), \tag{3}$$

where $\mathscr{V}$ is the kinematic viscosity, and β is the thermal expansion coefficient. Equations (1), (2-a), and (2-b) can be reduced to the following equations in terms of the stream function and vorticity:

$$\frac{\partial^2 \psi}{\partial x^2} + \frac{\partial^2 \psi}{\partial y^2} = -\omega, \tag{4}$$

$$u\frac{\partial \omega}{\partial x} + v\frac{\partial \omega}{\partial y} = \mathscr{V}\left(\frac{\partial^2 \omega}{\partial x^2} + \frac{\partial^2 \omega}{\partial y^2}\right) + g\beta\frac{\partial T}{\partial x}, \tag{5}$$

where ψ is the stream function, and ω is the vorticity.

To cast the governing equations into a dimensionless form, the following dimensionless variables are introduced:

$$\begin{aligned} &X = \frac{x}{H}, \quad Y = \frac{y}{H}, \\ &U = \frac{u}{\sqrt{g\beta(T_h - T_c)H}}, \quad V = \frac{v}{\sqrt{g\beta(T_h - T_c)H}}, \\ &\Omega = \frac{\omega}{\sqrt{g\beta(T_h - T_c)H^{-1}}}, \quad \Psi = \frac{\psi}{\sqrt{g\beta(T_h - T_c)H^3}}, \\ &\theta = \frac{T - T_c}{T_h - T_c}. \end{aligned} \tag{6}$$

Substituting the above dimensionless variables into the stream function, vorticity, and energy equations results in the following dimensionless form of the governing equations:

$$\frac{\partial^2 \Psi}{\partial X^2} + \frac{\partial^2 \Psi}{\partial Y^2} = -\Omega, \tag{7}$$

$$U\frac{\partial \Omega}{\partial X} + V\frac{\partial \Omega}{\partial Y} = \frac{1}{\sqrt{Gr}}\left(\frac{\partial^2 \Omega}{\partial X^2} + \frac{\partial^2 \Omega}{\partial Y^2}\right) + \frac{\partial \theta}{\partial X}, \tag{8}$$

$$U\frac{\partial \theta}{\partial X} + V\frac{\partial \theta}{\partial Y} = \frac{1}{\sqrt{RaPr}}\left(\frac{\partial^2 \theta}{\partial X^2} + \frac{\partial^2 \theta}{\partial Y^2}\right), \tag{9}$$

where Pr is the Prandtl number. The Rayleigh number Ra, and the Grashof number Gr are defined as:

$$Ra = \frac{g\beta(T_h - T_c)H^3}{\mathscr{V}\alpha}, \quad Gr = \frac{Ra}{Pr} \tag{10}$$

Subsequently, the boundary conditions for Eqs. (7) through (9) should be specified. Since the vorticity is not known on the boundaries of the cavity, to obtain the boundary condition for it, the truncated Taylor series expansion of the stream function for a point inside the cavity in the vicinity of the boundary is written as:

$$\Psi_{in} \cong \Psi_w + \left.\frac{\partial \Psi}{\partial t}\right|_w \Delta t + \left.\frac{\partial^2 \Psi}{\partial t^2}\right|_w \frac{\Delta t^2}{2} + \left.\frac{\partial \Psi}{\partial s}\right|_w \Delta s + \left.\frac{\partial^2 \Psi}{\partial s^2}\right|_w \frac{\Delta s^2}{2} + \left.\frac{\partial^2 \Psi}{\partial t \partial s}\right|_w \Delta t\ \Delta s, \quad (11)$$

where Ψ_{in} and Ψ_w are the values of the stream functions at a point inside the cavity next to the wall and on the wall, respectively. Also s and t denote the tangential and the normal directions to the wall, respectively. Writing equation (7) in the s-t coordinates system, and noting that Ψ remains constant along the walls yield:

$$\left.\frac{\partial^2 \Psi}{\partial s^2}\right|_w + \left.\frac{\partial^2 \Psi}{\partial t^2}\right|_w = -\Omega_w\ . \quad (12)$$

But on the other hand

$$\left.\frac{\partial \Psi}{\partial t}\right|_w = \sqrt{U_w^2 + V_w^2}\ , \quad (13)$$

where U_w and V_w are the components of the wall velocity in the X and Y-directions, respectively. Substituting relations (12) and (13) into Eq. (11) and, considering the fact that Ψ is constant along the walls result the appropriate relation (14) for the vorticity along the wall, Ω_w. The relation is in terms of the wall velocity components, and the stream functions both along the wall Ψ_w and at a point inside the cavity immediately next to the wall Ψ_{in}. Therefore,

$$\Omega_w = \frac{2}{\Delta t^2}\left(\sqrt{U_w^2 + V_w^2}\ \Delta t + \Psi_w - \Psi_{in}\right)\ . \quad (14)$$

Employing Eq. (14) for the vorticity along the walls, the boundary conditions for Eqs. (7-9) can now be shown in Fig. 1. In this study, the Prandtl number of the fluid is 0.71, and the Rayleigh numbers considered are 10^3, 10^4, 10^5 and 10^6.

3 Weak Formulation

In this present work, for the MLPG method implemented, an arbitrary collection of points is selected in the computational domain (Fig. 1). Subsequently, a control volume is generated around each of the points. The control volumes have simple shapes, such as, circle or rectangle in the two-dimensional space. The size of the control volumes, and the number of points belonging to each one of them can, in general, vary. Contrary to the conventional control volume techniques, in this method, the control volumes can intersect each other and overlap. A typical rectangular control volume generated around one of the nodes (node *I*) is shown in Fig. 1.

As the first step in developing the discretized equations for a control volume Ω_I, the weak forms of the governing equations are to be obtained. This is accomplished by multiplying the stream function, vorticity, and energy equations by the test function W$_I$ which is chosen to be unity in this study, ($W_I = 1$). The domain of the test function coincides with the control volume, i.e. the test function W$_I$ is equal to unity both inside and on the boundary of the considered control volume Ω_I, and will be zero otherwise. Subsequently, the resulting equations are integrated over Ω_I. After performing the integration by parts, the weak forms of the stream function, vorticity, and energy equations for the control volume Ω_I are expressed, respectively, as:

$$\int_{\Gamma_I-\Gamma_I\bigcap\Gamma_h} \frac{\partial\Psi}{\partial n} d\Gamma + \int_{\Gamma_I\bigcap\Gamma_h} \frac{\partial\Psi}{\partial n} d\Gamma = -\int_{\Omega_I} \Omega\, d\Omega\,, \tag{15}$$

$$\int_{\Omega_I} \left(U\frac{\partial\Omega}{\partial X} + V\frac{\partial\Omega}{\partial Y} \right) d\Omega = \frac{1}{\sqrt{Gr}} \int_{\Gamma_I-\Gamma_I\bigcap\Gamma_h} \frac{\partial\Omega}{\partial n} d\Gamma + \frac{1}{\sqrt{Gr}} \int_{\Gamma_I\bigcap\Gamma_h} \frac{\partial\Omega}{\partial n} d\Gamma + \int_{\Omega_I} \frac{\partial\theta}{\partial X} d\Omega\,, \tag{16}$$

$$\int_{\Omega_I} \left(U\frac{\partial\theta}{\partial X} + V\frac{\partial\theta}{\partial Y} \right) d\Omega = \frac{1}{\sqrt{Ra\,Pr}} \int_{\Gamma_I-\Gamma_I\bigcap\Gamma_h} \frac{\partial\theta}{\partial n} d\Gamma + \frac{1}{\sqrt{Ra\,Pr}} \int_{\Gamma_I\bigcap\Gamma_h} \frac{\partial\theta}{\partial n} d\Gamma\,, \tag{17}$$

where Γ_h is the portion of the domain boundary, where the natural boundary condition is enforced. Here, Γ_I is the boundary of the control volume Ω_I , and $\Gamma_I\bigcap\Gamma_h$ represents the intersection of Γ_I with Γ_h.

In the next step of the discretization process, the integrals in Eqs. (15-17) are to be evaluated. The Gaussian quadrature is employed for this purpose. To perform the numerical integrations, the control volume Ω_I is divided into a number of sub-partitions (Fig. 1). The proper number of the Gauss points for the surface and the contour integrations in each sub-domain are selected. Subsequently, the field variables ought to be approximated at each Gauss point. The MLS interpolation, which is described next, is employed for this purpose.

4 MLS Approximations

To obtain the discretized? equations, the unknown field variables have to be approximated at each Gauss point. The MLS interpolation is used for this purpose. Assuming Ω_k as the interpolation domain for a typical Gauss point, and S_j, $j = 1(1)n_k$, as a collection of n_k nodal points with coordinates $\widetilde{\mathbf{x}}_j \in \Omega_k$ (whose influence domains cover the considered Gauss point), the unknown stream function, vorticity, and temperature fields are approximated within Ω_k , respectively by

$$\Psi(\widetilde{\mathbf{x}}) \cong \overline{\Psi}^{(k)}(\widetilde{\mathbf{x}}) = \sum_{l=1}^{m} p_l(\widetilde{\mathbf{x}})\,\alpha_l = \mathbf{P}^T(\widetilde{\mathbf{x}})\,\boldsymbol{\alpha}\ , \tag{18a}$$

$$\Omega(\widetilde{\mathbf{x}}) \cong \overline{\Omega}^{(k)}(\widetilde{\mathbf{x}}) = \sum_{l=1}^{m} p_l(\widetilde{\mathbf{x}})\,\beta_l = \mathbf{P}^T(\widetilde{\mathbf{x}})\,\boldsymbol{\beta}, \tag{18b}$$

$$\theta(\widetilde{\mathbf{x}}) \cong \overline{\theta}^{(k)}(\widetilde{\mathbf{x}}) = \sum_{l=1}^{m} p_l(\widetilde{\mathbf{x}})\,\gamma_l = \mathbf{P}^T(\widetilde{\mathbf{x}})\,\boldsymbol{\gamma}. \tag{18c}$$

In Eqs. (18) $\boldsymbol{\alpha} = [\alpha_1, \alpha_2, \cdots, \alpha_m]^T$, $\boldsymbol{\beta} = [\beta_1, \beta_2, \cdots, \beta_m]^T$, and $\boldsymbol{\gamma} = [\gamma_1, \gamma_2, \cdots, \gamma_m]^T$ are vectors of the unknown coefficients, and $\mathbf{P}(x,y)$ is a known vector having m elements, $p_l(\widetilde{\mathbf{x}})$, $l = 1\ (1)\ m$, are, in general, monomials [Oñate, Idelsohn, Zienkiewicz, Taylor (1996)]. For example, for linear approximation of the field variables in the two-dimensional space, m is equal to 3 and the transpose of the vector $\mathbf{P}(x,y)$ is $\mathbf{P}^T(x,y) = [1, x, y]$.

Employing the MLS interpolation for $n_k > m$, the coefficient vector $\boldsymbol{\alpha}$ in Eq. (18-a) is determined by minimizing the following functional

$$J = \sum_{j=1}^{n_k} \varphi_j(\widetilde{\mathbf{x}} - \widetilde{\mathbf{x}}_j)[\hat{\Psi}_j - \mathbf{P}_j^T\boldsymbol{\alpha}]^2\ , \tag{19}$$

where $\mathbf{P}_j = \mathbf{P}(\widetilde{\mathbf{x}}_j)$, and also $\hat{\Psi}_j = \Psi(\widetilde{\mathbf{x}}_j)$, and $\varphi_j(\widetilde{\mathbf{x}} - \widetilde{\mathbf{x}}_j)$, $j = 1\,(1)\,n_k$, are the fictitious nodal values and the MLS weighting functions, respectively. Standard minimization yields

$$\boldsymbol{\alpha} = \mathbf{A}^{-1}\mathbf{B}\hat{\boldsymbol{\Psi}} \tag{20a}$$

where

$$\hat{\boldsymbol{\Psi}} = [\hat{\Psi}_1, \hat{\Psi}_2, \cdots, \hat{\Psi}_{n_k}]^T \tag{20b}$$

The matrices $\mathbf{A}$ and $\mathbf{B}$ in Eq. (20) are given by

$$\mathbf{A} = \sum_{j=1}^{n_k} \varphi_j(\widetilde{\mathbf{x}} - \widetilde{\mathbf{x}}_j)\mathbf{P}(\widetilde{\mathbf{x}}_j)\mathbf{P}^T(\widetilde{\mathbf{x}}_j)\ , \tag{21}$$

$$\mathbf{B} = \left[\varphi_1 \left(\widetilde{\mathbf{x}} - \widetilde{\mathbf{x}}_1\right) \mathbf{P}\left(\widetilde{\mathbf{x}}_1\right), \varphi_2 \left(\widetilde{\mathbf{x}} - \widetilde{\mathbf{x}}_2\right) \mathbf{P}\left(\widetilde{\mathbf{x}}_2\right), \cdots, \varphi_{n_k} \left(\widetilde{\mathbf{x}} - \widetilde{\mathbf{x}}_{n_k}\right) \mathbf{P}\left(\widetilde{\mathbf{x}}_{n_k}\right)\right] . \tag{22}$$

The coefficients $\boldsymbol{\beta}$ and $\boldsymbol{\gamma}$ are obtained by the same procedure as above, and are given by

$$\boldsymbol{\beta} = \mathbf{A}^{-1}\mathbf{B}\widehat{\boldsymbol{\Omega}}, \quad \boldsymbol{\gamma} = \mathbf{A}^{-1}\mathbf{B}\widehat{\boldsymbol{\theta}}. \tag{23}$$

Substituting the coefficients vectors $\boldsymbol{\alpha}, \boldsymbol{\beta}$, and $\boldsymbol{\gamma}$ from (20) and (23) into the relations (18-a), (18-b), and (18-c), respectively, yields the following approximations for the stream function, vorticity, and temperature within Ω_k :

$$\overline{\Psi}^{(k)}\left(\widetilde{\mathbf{x}}\right) = \sum_{j=1}^{n_k} N_j^{(k)}\left(\widetilde{\mathbf{x}}\right)\hat{\Psi}_j, \tag{24a}$$

$$\overline{\Omega}^{(k)}\left(\widetilde{\mathbf{x}}\right) = \sum_{j=1}^{n_k} N_j^{(k)}\left(\widetilde{\mathbf{x}}\right)\hat{\Omega}_j, \tag{24b}$$

$$\overline{\theta}^{(k)}\left(\widetilde{\mathbf{x}}\right) = \sum_{j=1}^{n_k} N_j^{(k)}\left(\widetilde{\mathbf{x}}\right)\hat{\theta}_j. \tag{24c}$$

Where $N_j^{(k)}\left(\widetilde{\mathbf{x}}\right)$, $j = 1(1)n_k$ are the MLS interpolation functions which are given by

$$N_j^{(k)}\left(\widetilde{\mathbf{x}}\right) = \sum_{l=1}^{m} p_l\left(\widetilde{\mathbf{x}}\right)\mathbf{D}_{lj}^{-1}, \quad j = 1\left(1\right)n_k, \tag{25}$$

where $\mathbf{D}^{-1} = \mathbf{A}^{-1}\mathbf{B}$.

5 Discretized Equations

Having found the weak formulations of the governing equations, and the moving least-squares (MLS) approximations of the field variables, the final step in the discretization process is to present the fully-discretized equations for an internal control volume Ω_I with the boundary Γ_I. For this purpose, the control volume Ω_I is divided to a number of sub-domains. The proper number of the Gauss points is selected in each of the sub-domains. Subsequently, the moving least-squares interpolations for the stream function, vorticity, and temperature (Eqs 24-a, b, c) at a typical Gauss point k are substituted into Eqs (15-17). The resulting discretized equations are given by:

$$\sum_{j=1}^{n_k}\left(\int_{\Gamma_I - \Gamma_I \cap \Gamma_h} N_{j,n}^{(k)}\left(\widetilde{\mathbf{x}}\right) d\Gamma\right)\hat{\Psi}_j = -\sum_{j=1}^{n_k}\left(\int_{\Omega_I} N_j^{(k)}\left(\widetilde{\mathbf{x}}\right) d\Omega\right)\hat{\Omega}_j - \int_{\Gamma_I \cap \Gamma_h} \frac{\partial \Psi}{\partial n} d\Gamma, \tag{26a}$$

$$\sum_{j=1}^{n_k}\left[\int_{\Omega_I}\left(UN^{(k)}_{j,X}(\widetilde{\mathbf{x}})+VN^{(k)}_{j,Y}(\widetilde{\mathbf{x}})\right)d\Omega-\frac{1}{\sqrt{Gr}}\int_{\Gamma_I-\Gamma_I\bigcap\Gamma_h}N^{(k)}_{j,n}(\widetilde{\mathbf{x}})\,d\Gamma\right]\hat{\Omega}_j=$$
$$\frac{1}{\sqrt{Gr}}\int_{\Gamma_I\bigcap\Gamma_h}\frac{\partial\Omega}{\partial n}d\Gamma+\int_{j=1}^{n_k}\left(\sum_{\Omega_I}N^{(k)}_{j,X}(\widetilde{\mathbf{x}})\,d\Omega\right)\hat{\theta}_j, \tag{26b}$$

$$\sum_{j=1}^{n_k}\left[\int_{\Omega_I}\left(UN^{(k)}_{j,X}(\widetilde{\mathbf{x}})+VN^{(k)}_{j,Y}(\widetilde{\mathbf{x}})\right)d\Omega-\frac{1}{\sqrt{Ra\,Pr}}\int_{\Gamma_I-\Gamma_I\bigcap\Gamma_h}N^{(k)}_{j,n}(\widetilde{\mathbf{x}})\,d\Gamma\right]\hat{\theta}_j=$$
$$\frac{1}{\sqrt{Ra\,Pr}}\int_{\Gamma_I\bigcap\Gamma_h}\frac{\partial\theta}{\partial n}d\Gamma\,. \tag{26c}$$

Similar discretized equations can be obtained for all the Gauss points of the control volume Ω_I and, in turn, for all the control volumes of the domain. Assembling these equations for the control volume, and enforcing the essential boundary conditions by the direct interpolation method yield a set of algebraic equations. Solving this system of the algebraic equations yields the unknown nodal values of the field variables.

6 Benchmarking of the Code

In order to validate the numerical procedure, a number of test cases are examined using the proposed code, and the results are compared with those of the analytical solutions, or compared with the existing numerical results in the literature.

The first test case considered is a heat conduction problem in a square domain. The domain, the boundary conditions, and a typical point distribution for the MLPG method implemented are shown in Fig. 2. The exact solution for the problem is $T_{exact}(x,y)=xy$. Figure 3 shows a comparison between the isotherms resulted by the code and those obtained from the analytical solution. As the figure shows excellent agreements are observed between the two. The variations of the L^2-norm for the error between the analytical and the numerical solutions with respect to the size of the control volumes are depicted in Fig. 4. The convergence of the MLPG obtained results with decreasing the size of the control volumes is demonstrated in this figure. As the figure shows the rate of the convergence is nearly quadratic.

The second test case considered is the heat conduction problem in a triangle domain. The domain, the boundary conditions, and the point distributions used for the numerical calculations for this test case are shown in Fig. 5. The exact solution

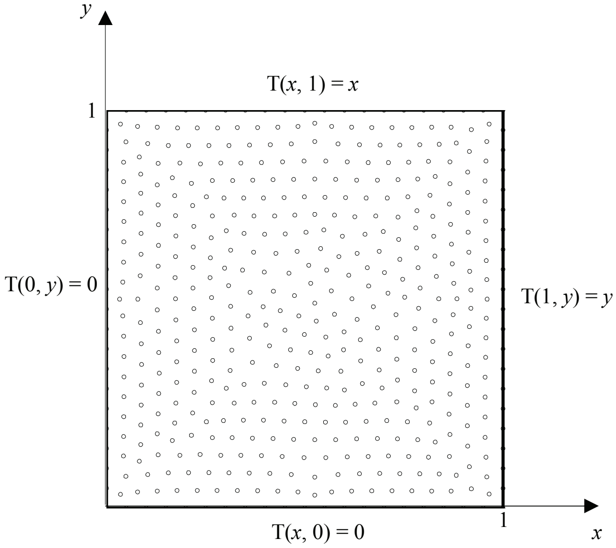

Figure 2: Square domain, boundary conditions, and point distributions

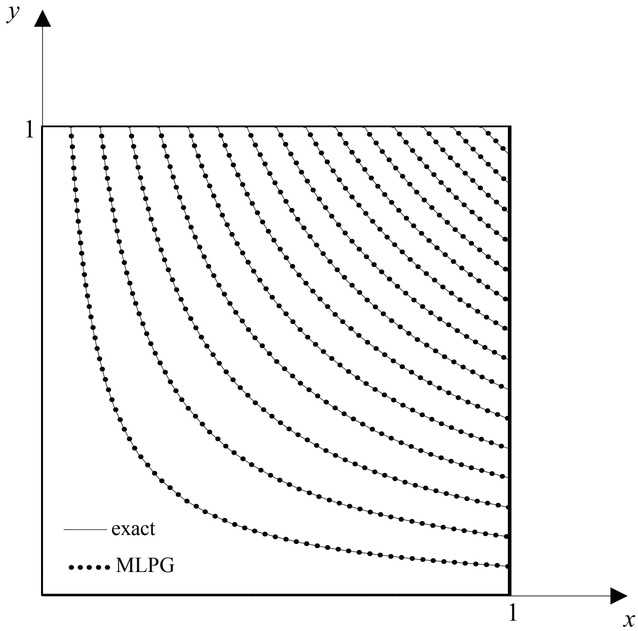

Figure 3: Isotherms for the square domain, a comparison with the exact solution

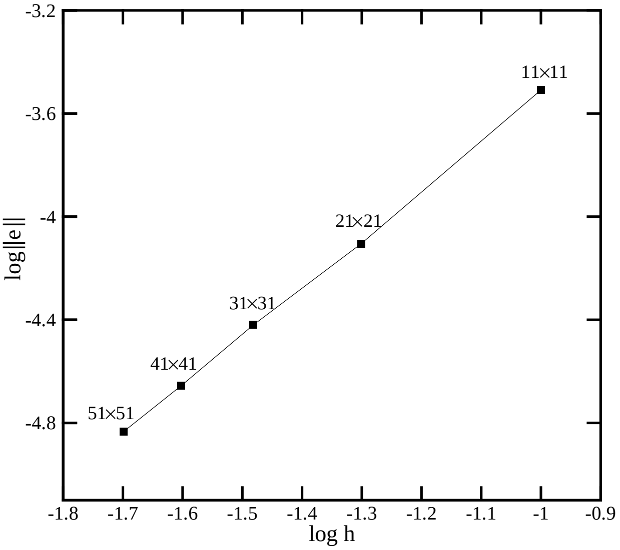

Figure 4: L^2-norm for the error between the analytical and the numerical solutions for different control volumes size

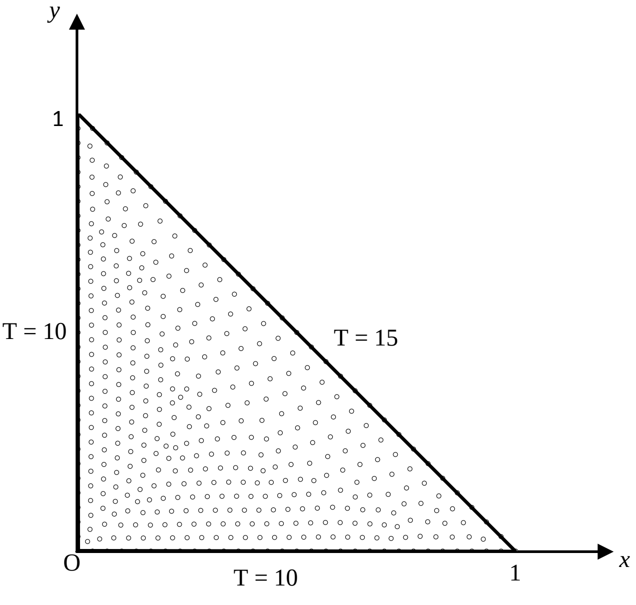

Figure 5: Triangle domain, boundary conditions, and point distributions

for the problem is [Greenberg (1978)]

$$T_{exact}\left(x,y\right) = 10+\frac{40}{\pi}\sum_{n=1,3,...}^{\infty}\left[\frac{\sinh(n\pi x)\sin(n\pi y)}{n\sinh(n\pi)}+\frac{\sinh(n\pi y)\sin(n\pi x)}{n\sinh(n\pi)}\right]. \quad (27)$$

Figure 6 shows the isotherms obtained using the proposed numerical simulation. The analytical isotherms depicted in this figure are for the comparison purposes. Again, as the figure shows, excellent agreements exist between the two results.

The third test case being considered here using the present code is the lid-driven cavity flow. The cavity is filled with air and the simulation is performed for Re = 10^3. The domain, the boundary conditions, and the point distributions are depicted in Fig. 7.

The streamlines for this case are presented in Fig. 8. Figure 9 shows the cavity's horizontal centerline velocity, U(0.5,Y), as well as, its vertical centerline velocity, V(X,0.5), as they are determined by the current simulation. The results of Ghia U; Ghia K.N; and Shin (1982) using the FVM are also presented in this figure for comparisons. Very good agreements are observed between the two results as the figure indicates.

As the fourth and final test case, the buoyancy-driven heat transfer in a differentially-heated square cavity being filled with air (Pr = 0.71) is considered (Fig. 10). The left and right walls of the cavity are maintained at constant temperatures T_h and T_c, respectively, with $T_h > T_c$. The top and bottom walls are insulated. The domain, the boundary conditions, and the point distributions are depicted in Fig. 10. The MLPG results are presented for some different Rayleigh numbers ranging from 10^3 to 10^6. Table 1 shows the comparisons between the maximum values of the velocity components, their locations, and the average Nusselt numberS on the hot wall obtained using the present numerical simulation with those of other investigators. As it can be seen from the table, very good agreements exist between the implemented code and the results of the other investigators for the entire range of the Rayleigh numbers considered.

7 Results and Discussions

Having verified the present code performance via solving different test cases, the code was employed to investigate the characteristics of the buoyancy-driven fluid flow and heat transfer in cavities having wavy walls. Two different cases were considered: a cavity having a single wavy wall on one of its sides, and a cavity having two wavy walls on both of its sides. In the former case, the wavy wall (on

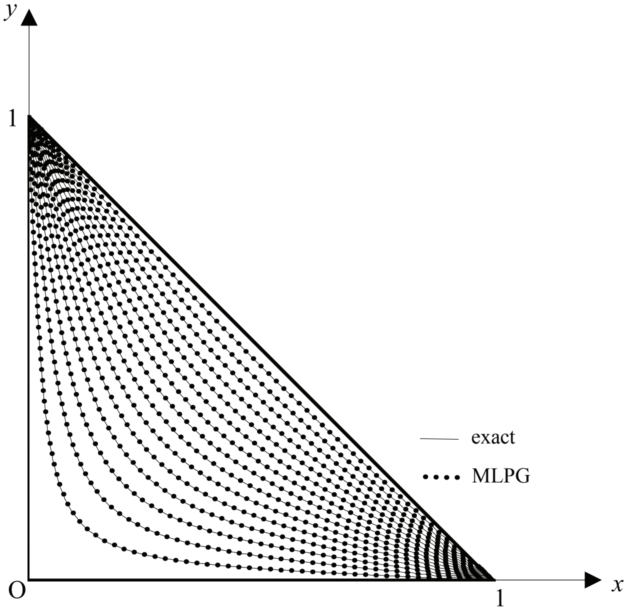

Figure 6: Isotherms with arbitrary distributed points, a comparison with the analytical solution

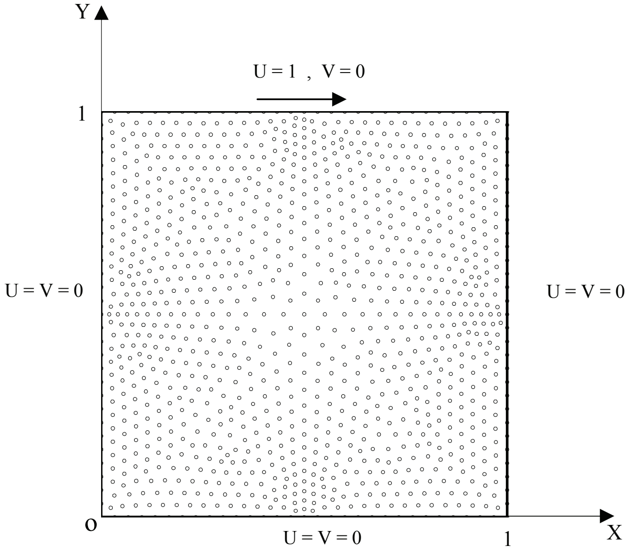

Figure 7: Domain, boundary conditions, and point distribution for lid-driven cavity flow

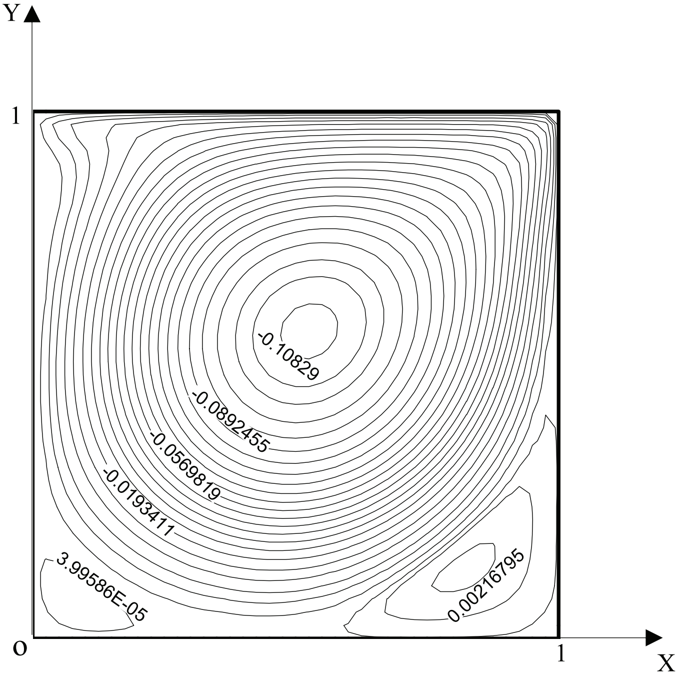

Figure 8: Streamlines for the lid-driven cavity flow, Re = 10^3

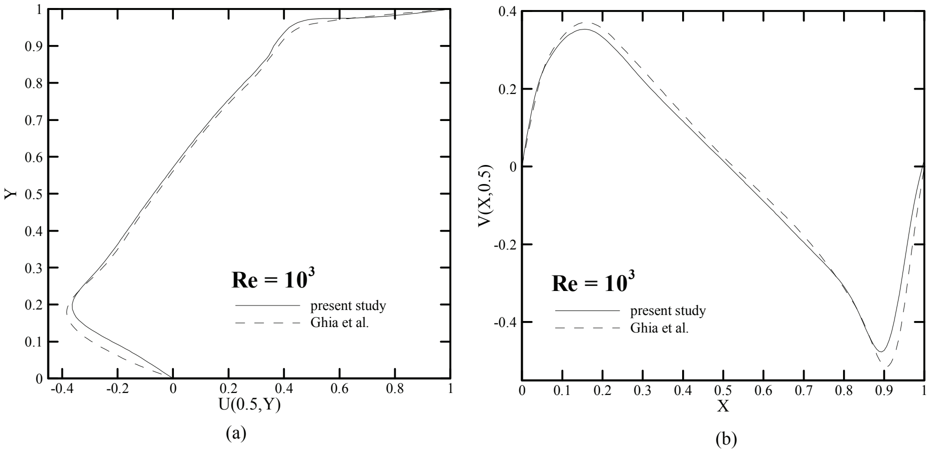

(a)

(b)

Figure 9: Centerlines velocities for lid-driven cavity flow, comparison of MLPG method with FVM results: (a) U(0.5,Y), (b) V(X,0.5)

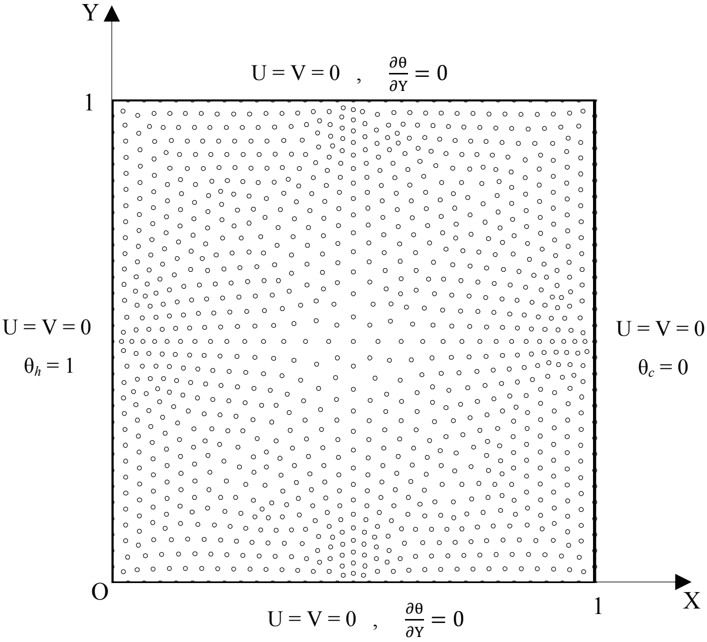

Figure 10: Domain, boundary conditions, and point distribution for the buoyancy-driven flow in a differentially heated cavity, Pr = 0.71

the left side) is described by the following equation

$$x_{left} = \frac{A}{2}\left(1 - \cos\left(2n_A \pi y\right)\right), \tag{28}$$

where, A is a amplitude, and n_A is the number of wall undulations. For the two wavy walls case, two different situations as far as the erections of the walls, were considered. First the two walls were erected in such a way that they were symmetric with respect to the vertical centerline of the cavity, and next, when the two walls were located antisymmetrically with respect to the same centerline. These two cavities are hereafter referred to as the symmetrical and antisymmetrical configurations, respectively. In the symmetrical-configuration, the left and the right wavy walls are described, respectively, by:

$$x_{left} = \frac{A}{2}\left(1 - \cos\left(2n_A \pi y\right)\right), \tag{29a}$$

$$x_{right} = 1 + \frac{A}{2}\left(-1 + \cos\left(2n_A \pi y\right)\right). \tag{29b}$$

Table 1: Comparison of the code results with those of other investigators for natural convection in a square cavity, (Pr = 0.71), U_{max} at Y = 0.5, V_{max} at X = 0.5

Markatos	**Khanafer**	**Fusegi**	**Davis**	**Barakos**	**present study**		
-	0.137	0.132	0.136	0.153	0.134	U_{max}	Ra $=10^3$
0.832	0.812	0.833	0.813	0.806	0.800	Y_{Umax}	
-	0.139	0.131	0.138	0.155	0.135	V_{max}	
0.168	0.173	0.200	0.178	0.181	0.200	X_{Vmax}	
1.108	1.118	1.105	1.118	1.114	1.175	Nu_{avg}	
-	0.192	0.201	0.192	0.193	0.192	U_{max}	Ra $=10^4$
0.832	0.827	0.817	0.823	0.818	0.800	Y_{Umax}	
-	0.233	0.225	0.234	0.234	0.223	V_{max}	
0.113	0.123	0.117	0.119	0.119	0.150	X_{Vmax}	
2.201	2.245	2.302	2.243	2.245	2.374	Nu_{avg}	
-	0.131	0.147	0.153	0.132	0.140	U_{max}	Ra $=10^5$
0.857	0.854	0.855	0.855	0.859	0.866	YU_{Umax}	
-	0.258	0.247	0.261	0.258	0.240	V_{max}	
0.067	0.065	0.065	0.066	0.066	0.067	X_{Vmax}	
4.430	4.522	4.646	4.519	4.510	4.761	Nu_{avg}	
-	0.077	0.084	-	0.077	0.085	U_{max}	Ra $=10^6$
0.872	0.854	0.856	0.872	0.859	0.833	Y_{Umax}	
-	0.262	0.259	-	0.262	0.268	V_{max}	
0.038	0.039	0.033	0.038	0.039	0.033	X_{Vmax}	
8.754	8.826	9.012	8.799	8.806	9.204	Nu_{avg}	

For the antisymmetrical-configuration, the equation of the left wall is the same as before, but the right wall is described by:

$$x_{right} = 1 + \frac{A}{2}\left(1 - \cos\left(2n_A \pi y\right)\right). \tag{30}$$

In the followings, the effects of the pertinent parameters such as, the number of undulations of the wavy walls, the dimensionless amplitudes, and the Rayleigh number on the natural convection inside the appropriate cavities are investigated and discussed. All the presented materials here are for air as the working fluid with Pr = 0.71.

7.1 Single Wavy Wall

The streamlines for a cavity with a left (hot) wavy wall, having only one undulation for three different dimensionless amplitudes for Ra = 10^5 are shown in Fig. (11-a). The respective isotherms are depicted in Fig. (11-b). The existence of distinct boundary layers near the side-walls is clearly observed from Fig. (11). The heat transfer in the stratified core of the cavity occurs mainly through conduction as it can be seen from nearly parallel isotherms in the region. The variations of the local Nusselt numbers along the hot wall in this case for different dimensionless amplitudes are presented in Fig. (12). The results for the case of a flat hot wall (A = 0) are also shown in this figure. As the figure shows, for a flat hot wall the maximum Nusselt number occurs at the bottom left of the cavity. However, for a wavy hot wall, the natural convection weakens close to the bottom left corner of the cavity due to the flow blockage by the wall protrusion. Therefore, the local Nusselt number decreases somewhat in this region (Fig. (12)). Similar trend is observed for different amplitudes. Nevertheless, the effects of the blocking the fluid flow by the wavy wall intensifies with increasing the amplitude which results in a reduction of the maximum value of the Nusselt number (Fig. (12)). Moreover, as it can be seen from Fig. (11), the isotherms converge in the direction of the wall by moving towards the crest of the wave. Consequently, the maximum Nusselt number occurs somewhere before the crest. By continuing to move in the upwards direction, the isotherms begin to diverge, hence, the Nusselt number decreases steadily. The minimum value of the Nusselt number occurs at the top left corner of the cavity. The magnitude of the minimum Nusselt number is lower than that of a flat wall as a result of the depression of the wavy wall in this region.

The streamlines and the isotherms for a cavity having a hot wavy wall with three undulations are shown in Fig. (13-a) and (13-b), respectively. All the other conditions in these figures are similar to those in Fig. (11). The local Nusselt number distributions along the wavy wall for this case for the three amplitudes are shown in Fig. (14). It is observed from Fig. (13) that the isotherms converge towards the crests of the wavy wall, but by moving towards the troughs the flow weakens and the isotherms diverge. Consequently, as it can be seen from Fig. (14), the local maxima and the local minima of the Nusselt numbers distributions occur at the appropriate crests and troughs, respectively. The phenomenon, therefore, makes each Nusselt number distribution have the same frequency as that of the wavy wall itself.

With increasing the amplitudes, the flow and the natural convection weaken close to the left bottom corner of the cavity (Fig. (14)). Hence, the local Nusselt number decreases sharply in this region. Moreover, with increasing the amplitudes, the isotherms get more packed close to the crests and get further apart near the troughs. Hence, in turn, the magnitudes of the local maxima and the local min-

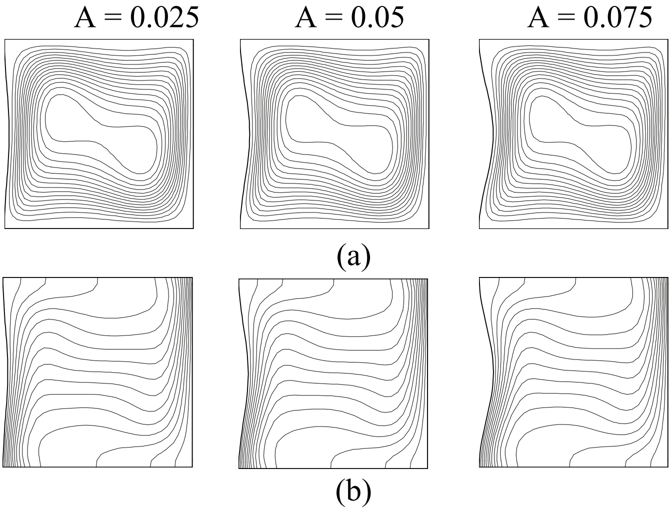

Figure 11: Streamlines (a), isotherms (b) for a cavity with a hot, one undulation wavy wall, Ra = 10^5

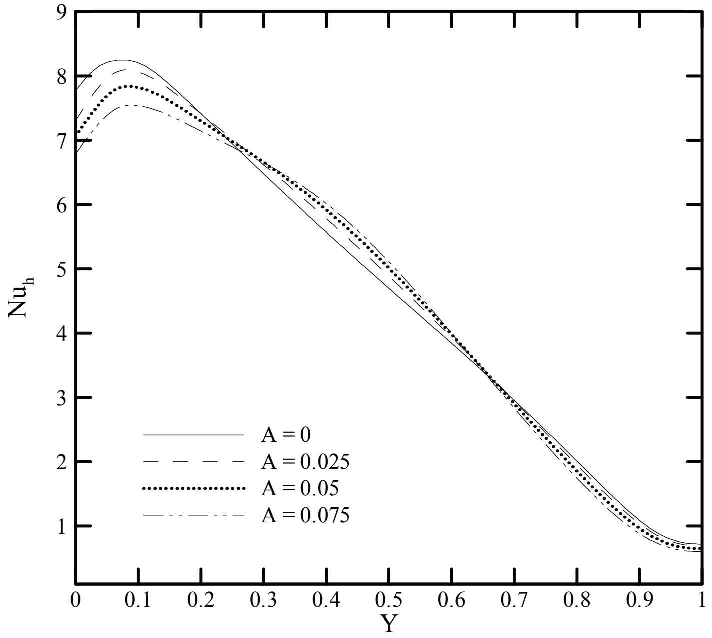

Figure 12: Local Nusselt number variations along the hot wavy wall with one undulation, Ra = 10^5

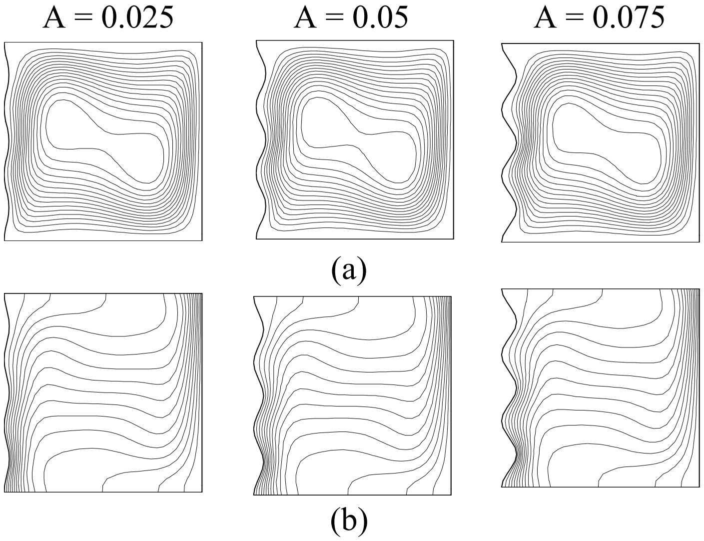

Figure 13: Streamlines (a), isotherms (b) for a cavity with a hot, three undulations wavy wall, Ra = 10^5

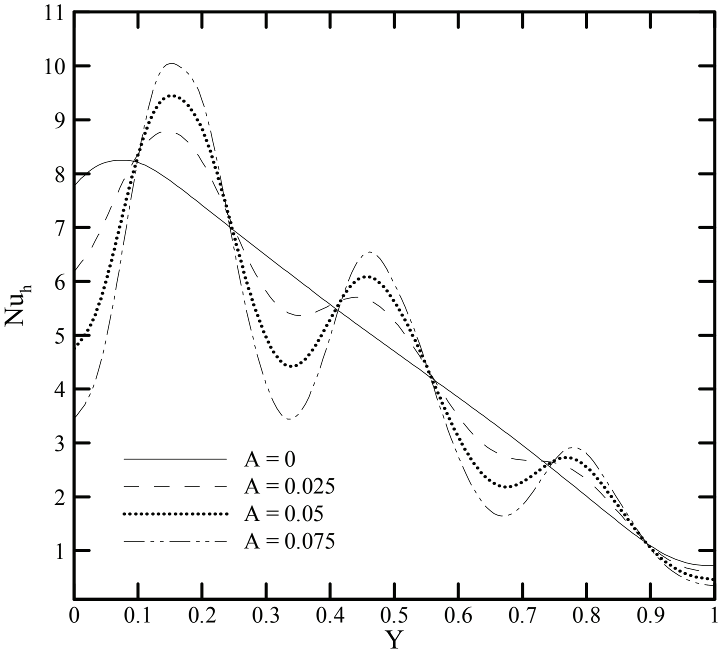

Figure 14: Local Nusselt number variations along the hot wavy wall with three undulations, Ra = 10^5

ima of the Nusselt numbers distributions increase and decrease, respectively, (Fig. (14)). However, by moving towards the top wall of the cavity, the difference between the temperature of the hot wall and the bulk fluid temperature decreases. Therefore, the difference between the local maxima and the local minima of the Nusselt number decreases as it is observed from Fig. (14).

Comparisons between the results of the present simulations for the local Nusselt number along the wavy wall of the cavities for the one and three undulations and the results of the finite volume method, carried out in this study only for verifications purposes, are presented in Fig. (15). The results are for the dimensionless amplitude of 0.05, and Ra = 10^5. Very good agreements are observed between the two results (Fig. (15)).

Figures (16-a) and (16-b) show the streamlines and the isotherms for a cavity having a wavy hot wall with five undulations, respectively. The results are presented for the same amplitudes and Rayleigh numbers as before. The local Nusselt number distributions along the wavy wall for these cases are depicted in Fig. (17). As it can be seen from Fig. (16), similar to the three undulations case, the isotherms converge and diverge close to the crests and the troughs, respectively. Again, the local Nusselt number distributions posses the same frequencies as those of the wavy walls. It is also observed from Fig. (17), that the local minima and the local maxima of each Nusselt number distribution increase and decrease, respectively, with increasing the number of undulations for each of the wavy wall. Moreover, the effect of the amplitude of the wavy wall on the local Nusselt number intensifies with increasing the number of undulations.

7.2 Double Wavy Walls

The present study is now extended to focus on the natural convection in a cavity with double wavy walls, one on each side of the considered cavity as shown in Fig. 1. The analyses are carried out for the two different configurations of the wavy walls set ups (the symmetrical and antisymmetrical, as explained earlier). All the results presented here are for wavy walls having three undulations and Ra = 10^5 unless stated otherwise.

The streamlines and the isotherms for the double wavy wall cavity having the symmetrical- configuration for different amplitudes are shown in Figs. (18-a) and (18-b), respectively. As it can be seen from the figures, similar to the case of the cavity with the single wavy wall, the isotherms converge and diverge towards the crests and the troughs, respectively. Moreover, the streamlines and the isotherms are inverse-symmetric with respect to the vertical centerline of the cavity. The local Nusselt number distributions along the hot wall for the double wavy wall with the symmetrical configuration are shown in Fig. (19a). The variations of the local

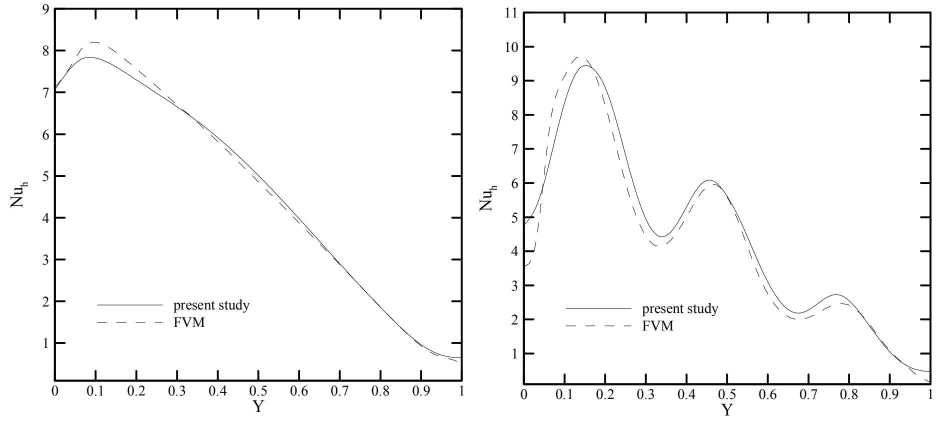

(a)

(b)

Figure 15: Comparisons between the local Nusselt number, the present simulation and the finite volume method for A = 0.05 and Ra = 10^5: (a) one undulation (b) three undulations

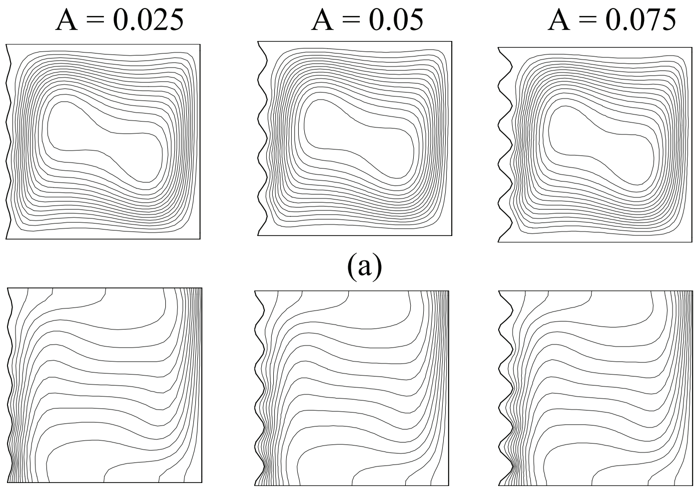

(a)

(b)

Figure 16: Streamlines and isotherms for a cavity with a hot wavy wall having five undulations, Ra = 10^5: (a) streamlines (b) isotherms

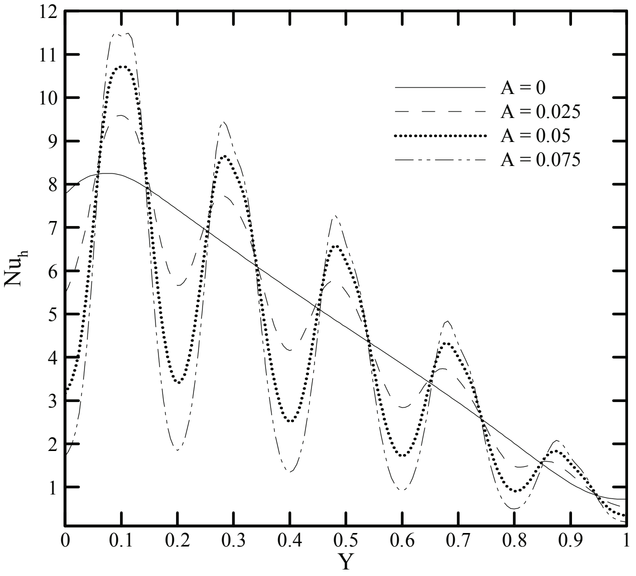

Figure 17: Local Nusselt number along the hot wavy wall having five undulations, Ra = 10^5

Nusselt number distribution along the hot wall for each amplitude is similar to that of the respective amplitude for the single wavy wall (Fig. 14). However, for the symmetrical configuration case (double wavy walls), since the cold wall faces the hot wall symmetrically, a local Nusselt number distribution similar to that of the hot wall is obtained for the cold wavy wall as depicted in Fig (19b).

Figures (20-a) and (20-b) show the streamlines and the isotherms for the cavity having the antisymmetrical-configuration of double wavy walls for different amplitudes, respectively. The variations of the local Nusselt number distributions along the hot and the cold walls for these cases are depicted in Figs. (21-a) and (21-b), respectively. As it can be observed from Fig. (20), the streamlines and the isotherms converge in the close proximity of the crests and diverge as they move towards the troughs of the wavy walls. Consequently, the local maxima and the local minima of the Nusselt numbers distributions occur close to the hills and the valleys of the wavy walls. The Nusselt number for each wavy wall has the same frequency as that of the wall itself (Fig. (21)). Moreover, contrary to the symmetrical-configuration, the Nusselt numbers distributions in this configuration of the wavy walls are not symmetric with respect to each other.

The average Nusselt numbers of the hot wall for the three cavities having a single

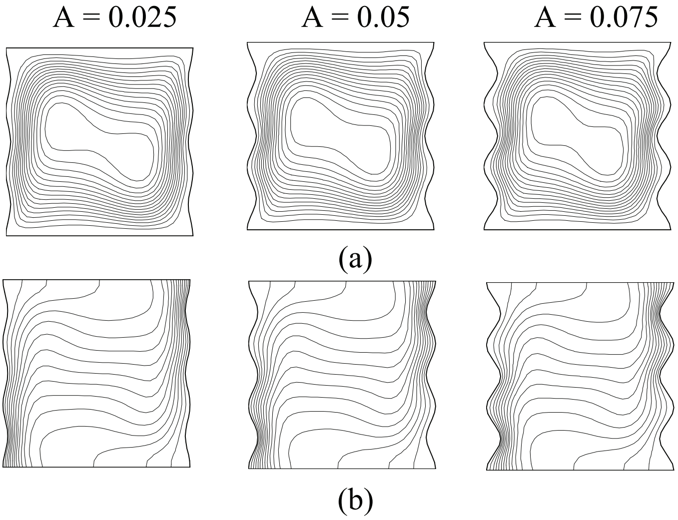

Figure 18: Streamlines and isotherms for a cavity having the symmetrical-configuration of double wavy walls, Ra = 10^5: (a) streamlines (b) isotherms

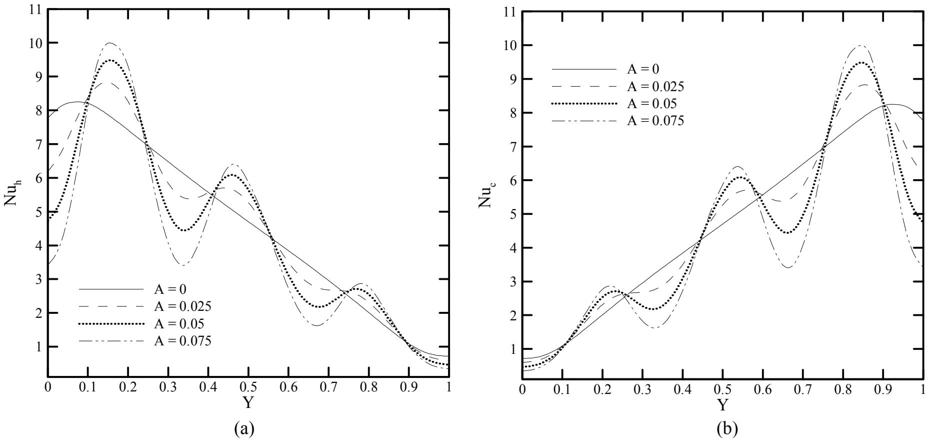

Figure 19: Local Nusselt number along the wavy walls for a double wavy wall cavity with the symmetrical-configuration, Ra = 10^5: (a) hot left wall (b) cold right wall

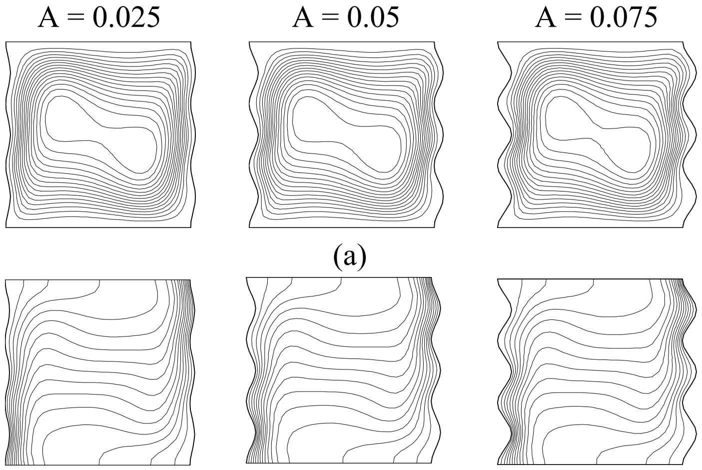

(a)

(b)

Figure 20: Streamlines and isotherms for a cavity having the antisymmetrical-configuration of double wavy walls, Ra = 10^5: (a) streamlines (b) isotherms

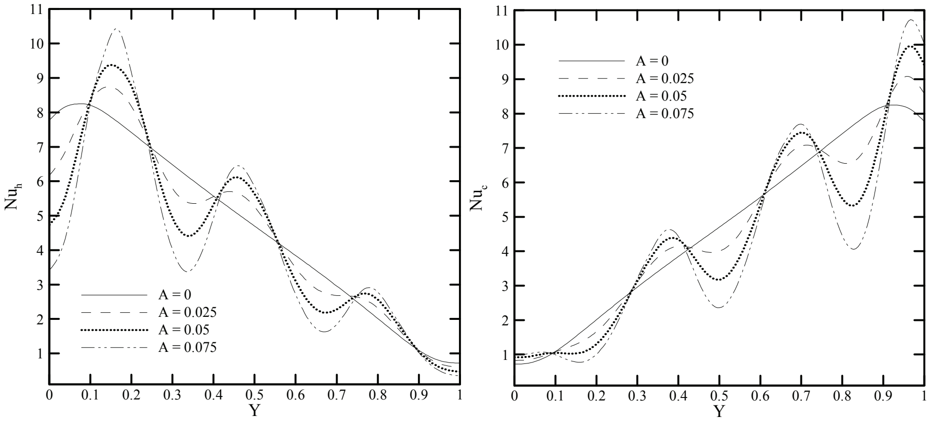

(a)

(b)

Figure 21: Local Nusselt number along the wavy walls for a double wavy wall cavity with the antisymmetrical-configuration, Ra = 10^5: (a) hot left wall (b) cold right wall

wavy wall (left wall), and the two configurations of the double wavy walls are presented in Table 2. The results in the table are for one, three, and five undulations, different amplitudes, and Ra = 10^5. It is seen from these results that, in all the cases, the average Nusselt number decreases with increasing both the amplitude and the number of undulations of the wavy walls. The average Nusselt numbers for all the cases in the table are lower than 4.761 which is the average Nusselt number of a square cavity filled with air for Ra = 10^5. Moreover, the average Nusselt number of the hot wall for the antisymmetrical-configuration of the double wavy walls is, in general, higher than that of the symmetrical-configuration. As the results show, for a fixed number of undulations, the average Nusselt number for all the cases decreases with increasing the amplitude. This behavior is attributed to the fact that increasing the amplitude intensifies the flow resistance, hence, diminishing the mass flow rate. This, in turn, reduces the rate of the heat transfer, considering a constant temperature difference between the hot and cold walls, and the buoyancy as the only driving force.

Table 2: Average Nusselt number of the hot wall for different undulations, amplitudes, and Ra = 10^5

Average Nusselt numbers			
A = 0.075	A = 0.05	A = 0.025	number of undulations
single wavy wall			
4.678	4.723	4.750	1
4.345	4.561	4.720	3
3.955	4.278	4.637	5
double wavy walls- symmetrical configuration			
4.625	4.709	4.737	1
4.291	4.537	4.715	3
3.877	4.243	4.635	5
double wavy walls- antisymmetrical configuration			
4.691	4.731	4.751	1
4.385	4.592	4.739	3
3.982	4.300	4.660	5

The effects of the Rayleigh number on the local Nusselt numbers of the hot wall for the two cavities having the symmetrical and antisymmetrical configurations of double wavy walls are shown in Fig. (22). The results are presented for Ra = 10^3, 10^4, 10^5, and 10^6. For Ra = 10^3, the heat transfer inside the cavities is conduction-dominated. Consequently, the isotherms in the middle of the cavity are nearly vertical. The distance between the hot wavy wall, which itself is an isotherm, and the isotherm at the middle of the cavity increases and decreases by moving towards the troughs and the crests of the wavy wall, respectively. Hence, the local maxima and the local minima of the Nusselt numbers occur at the crests and the troughs, respectively (Fig. (22)). Of course, by moving towards the top wall of the cavity, the difference between the wall and the bulk fluid temperature decreases. Consequently, the amplitude of the Nusselt number variation decreases somewhat towards the top of the cavity (Fig. (22)). With the increase of the Rayleigh number, the natural convection inside the cavity intensifies. Therefore, the magnitudes of the local maxima and the local minima of the Nusselt number distributions increase substantially for high Rayleigh numbers. As Fig. 22 shows, for all the Rayleigh numbers, the Nusselt number frequency is the same as the wall frequency itself.

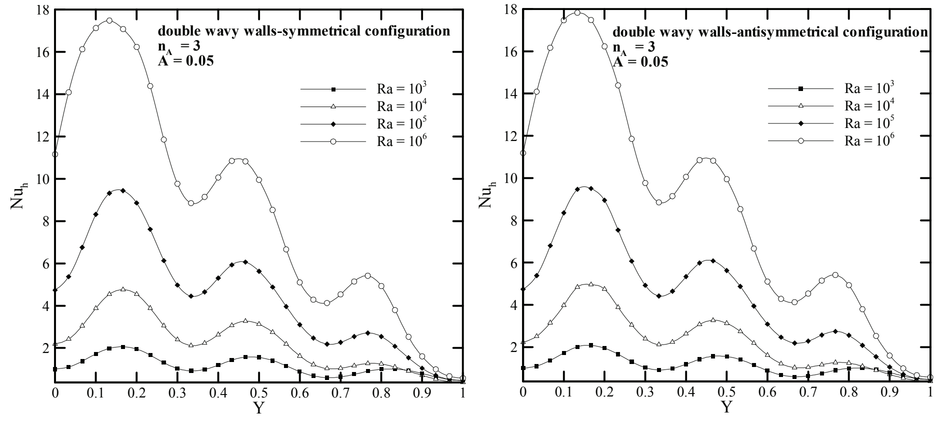

(a) (b)

Figure 22: Effects of Rayleigh number on the local Nusselt number for the hot wall for the two configurations (a) symmetrical (b) antisymmetrical

8 Conclusions

Since one of the most important advantages of the meshless techniques may be thought as its applicability for analyses of the fluid flow and heat transfer within irregular and or complex domains, achieving the MLPG scheme fulfilling this advantage might be considered as an important task for many investigators in the field. In this study the MLPG method has been extended to be utilized to simulate a buoyancy-driven fluid flow and heat transfer in cavities of some complex geometries such as the wavy walls enclosures. To verify the applicability of the method on such complex domains, the code was initially implemented on some types of enclosures having single wavy walls for which the appropriate data were obtained through other numerical techniques such as the conventional FVM. Having verified the applicability of the code, the scheme was then implemented on the natural convection heat transfer mode for enclosures having wavy walls on the two sides of the considered domains. Like the single wavy wall enclosures, the double wavy walls cases were examined for different wall's undulations, different amplitudes, and different Rayleigh numbers effects. For all the simple and complex cavities considered in this study, the MLPG method gave results which are in excellent agreements with those available in the literature and or what the logical trends have to be. Based on these findings, the total merits of the applicability of the MLPG method for the complex and irregular geometries as the basis for further exploration of the MLPG method implementations become obvious. Among the industrial applications of the method, one can think of the design of heat exchangers, solar collectors, nuclear reactors, and others.

References

Adjlout, L.; Imine, O., Azzi, A.; Belkadi, M. (2002): Laminar natural convection in an inclined cavity with a wavy wall. *Int. J. Heat and Mass Transfer*, Vol. 45, pp. 2141-2152.

Al-Amiri, A.; Khanafer, K; Bull, J.; Pop, I. (2007): Effect of the sinusoidal wavy bottom surface on mixed convection heat transfer in a Lid-driven cavity. *Int. J, Heat and Mass Transfer*, Vol.50, pp. 1771-1780.

Arefmanesh, A.; Najafi, M.; Abdi, H. (2005): A meshless local Petrov-Galerkin method for fluid dynamics and heat transfer applications. *J. of fluids Eng.*, Vol. 127, pp. 647-655.

Atluri, S.N. (2004): The meshless method (MLPG) for domain and bie discretization. Tech. Science Press, USA.

Atluri, S.N.; Shen, S. (2002): The meshless local Petrov-Galerkin (MLPG) method. Tech. Science Press, USA.

Atluri, S.N.; Zhu, T. (1998): A New Meshless Local Petrov-Galerkin (MLPG) Approach in Computational Mechanics. *Computational Mechanics*, Vol.22, pp. 117-127.

Atluri, S.N.; Zhu, T. (1998): A New Meshless Local Petrov-Galerkin (MLPG) Approach to Nonlinear

Problems in Computer Modeling & Simulation. *Computer Modeling & Simulation in Engg.*, Vol. 3, pp.187-196.

Atluri, S.N.; Zhu, T. (2000): A new meshless local Petrov-Galerkin (MLPG) approach for solving problems in elasto-statics. *Comput. Mech.*, Vol. 25, pp. 169 - 179.

Avila, R.; Perez, A. (2008): A Pressure Correction Approach Coupled with the MLPG Method for the Solution of the Navier-Stokes Equations. *Lectures notes in computational science and engineering 2008, Meshfree Method for partial differential equation IV*, pp. 19-32.

Barakos, G.; Mitsoulis, E. (1994): Natural convection flow in a square cavity revisited: laminar and turbulent models with wall functions. *Int. J. Numer. Methods Fluids*, vol.18, pp. 695-719.

Belytschko, T.; Krongauz, Y.; Organ, D.; Flemming, M.; Krysl, P. (1996): Meshless method: an overview and recent development. *Comput. Meth. Appl. Mech. Eng.*, Vol. 139, pp. 3-47.

Ching, H.K.; Chen, J.K. (2006): Thermomechanical analysis of functionally graded composites under laser heating by the MLPG method. *CMES: Computer Modeling in Engineering & siences,*Vol.13, no. 3, pp. 199- 218.

Das, P.K.; Mahmud, S. (2003): Numerical investigation of natural convection inside a wavy enclosure. *Int. J. Thermal sciences*, Vol. 42, pp. 397-406.

Dehghan, M.; Mirzaei, D. (2009): Meshless Local Petrov–Galerkin (MLPG) method for the unsteady magnetohydrodynamic (MHD) flow through pipe with arbitrary wall conductivity. *Applied Numerical Mathematics*, vol.59, pp.1043–1058.

De Vahl Davis, G. (1983): Natural convection of air in a square cavity a benchmark numerical solution. *Int. J. Numer. Methods Fluids*, vol. 3, pp. 249-264.

Fusegi, T.; Hyun, J.M.; Kuwahara, K.; Farouk, B. (1991): A numerical study of three-dimensional natural convection in a differentially heated cubical enclosure. *Int. J. Heat Mass Transfer*, vol.34, pp.1543-1557.

Ghia, U.; Ghia, K.N.; Shin, C.T. (1982): High-Re solution For Incompressible Flow Using the Navier-Stokes equations and the Multigrid Method. *J. computational physics*, vol. 48, pp. 387-411.

Greenberg, M.D. (1978): Foundations of Applied Mathematics. Prentice-Hall, Englewood Cliffs, NJ.

Haji Mohammadi, M. (2008): Stabilized Meshless Petrov-Galerkin Method (MLPG) for Incompressible Viscous Fluid Flows. *CMES: Computer Modeling in Engineering & Sciences*, vol.29, no.2, pp.75-94.

Han, Z.D; Liu, H.T; Rajendran, A.M.; Atluri, S.N. (2006): The applications of meshless local Petrov-Galerkin (MLPG) approaches in high-speed impact, penetration and perforation problems. *CMES: Computer Modeling in Engineering & Sciences*. vol. 14, no. 2, pp. 119-128.

Khanafer, K.; Vafai, K.; Lightstone, M. (2003): Buoyancy-driven heat transfer enhancement in a two-dimensional enclosure utilizing nanofluids. *Int. J. Heat Mass Transfer*, vol. 46, pp. 3639-3653.

Lin, H.; Atluri, S.N. (2000): Meshless local Petrov-Galerkin (MLPG) method for convection-diffusion problems. *CMES: Computer Modeling in Engineering & Sciences*, Vol. 1, no. 2, pp.45-60.

Lin, H.; Atluri, S.N. (2001): The meshless Local Petrov-Galerkin (MLPG) method for solving incompressible Navier-Stokes equations. *CMES: Computer Modeling in Engineering & Sciences*, Vol. 1, no. 2, pp.117-142.

Liu, G.R. (2003): Meshfree method moving beyond the finite element method. *CRC press*, USA.

Liu, L.H. (2006): Meshless method for radiation heat transfer in graded index medium. *Int. J. Heat Mass Transfer*, Vol. 44, pp. 214-229.

Lu, Y.Y.; Belytschko, T.; Gu, L. (1994): A new implementation of the element-free Galerkin Method. *Comput. Meth Appl. Mech. Eng.*, Vol. 113, pp. 397-414.

Ma, Q.W. (2005): MLPG Method Based on Rankine Source Solution for Simulating Nonlinear Water Waves. *CMES: Computer Modeling in Engineering & Sciences.* Vol. 9, no. 2, pp. 193-209.

Ma, Q.W. (2007): Numerical Generation of Freak Waves Using MLPG_R and QALE-FEM Methods. *CMES: Computer Modeling in Engineering & Sciences.* Vol. 18, no. 3, pp. 223-234.

Markatos, N.C.; Pericleous, K.A. (1984): Laminar and turbulent natural convection in an enclosed cavity. *Int. J. Heat Mass Transfer*, vol. 27, pp. 772-775.

Nayroles, B.; Touzot, G.; Villon, P. (1992): Generalizing the FEM: Diffuse Approximation and Diffuse Elements. *Comput. Mech*, Vol. 10, pp. 307-318.

Oñate, E.; Idelsohn, S.; Zienkiewicz, O.Z.; Taylor, R.L. (1996): A finite point method in computational mechanics: Applications to convective transport and fluid flow. *Int. J. Numer. Methods Eng.*, Vol.39, pp. 3839-3867.

Sabeur-Bendehina, A.; Adjlout, L.; Imine, O. (2006): Effect of Sinusoidal Distribution of the Temperature on Laminar Natural Convection in Wavy Rectangular Enclosures. *J. of Applied Sciences*, Vol. 6, no. 3, pp. 710-715.

Sadat, H.; Couturier, S. (2000): Performance and accuracy of a meshless method for laminar natural convection. *Numerical Heat Transfer*, Part B, Vol. 37, pp. 455-467.

Saha, S.; Sultana; T., Saha, G.; Rahman, M.M. (2008): Effects of discrete isoflux heat source size and angle of inclination on natural convection heat transfer flow inside a sinusoidal corrugated enclosure. *Int. J. Heat Mass Transfer,* Vol. 35, pp. 1288–1296.

Sellountos, E.J.; Vavourakis, V.; Polyzos, D. (2005): A new singular hypersingular MLPG (LBIE) method for 2d elastostatics. *CMES: Computer Modeling in Engineering & Sciences.* Vol. 6, no. 5, pp. 477-490.

Shi, X.; Khodadadi, M.J. (2003): Laminar Natural Convection Heat Transfer in a Differentially Heated Square cavity Due to a Thin Fin on The Hot Wall. *Journal of Heat Transfer*, Vol. 125, pp. 624-634.

Shu, C.; Ding, H.; Yeo, K.S. (2005): Computation of Incompressible Navier-Stokes Equations by Local RBF-based Differential Quadrature Method. *CMES: Computer Modeling in Engineering & Sciences*, Vol. 7, No. 2, pp. 195-206.

Sladek, J.; Sladek, V.; Atluri, S.N. (2004): Meshless local Petrov-Galerkin method for heat conduction problem in an anisotropic medium. *CMES: Computer Modeling in Engineering & Sciences*, Vol. 6, no. 2, pp.309-318.

Sladek, J.; Sladek, V.; Hellmich, Ch.; Eberhardsteiner, J. (2007): Heat conduction analysis of 3-D axisymmetric and anisotropic bodies by meshless local Petrov-Galerkin method. *Comput. Mech.*, Vol. 39, pp. 323-333.

Sladek, J.; Sladek, V.; Wen, P. H.; Aliabadi, M.H. (2006): Meshless local Petrov-Galerkin (MLPG) method for shear deformation shell analysis. *CMES: Computer Modeling in Engineering & Sciences.* Vol. 13, no. 2, pp. 103-108.

Sladek, J.; Sladek, V.; Zhang, Ch.; Solek, p.; Starek, L. (2007): Fracture analyzes in continuously nonhomogenous piezoelectric solid & the MLPG. *CMES: Computer Modeling in Engineering & Sciences.* Vol. 19, no. 3, pp. 247-262.

Sophy, T.; Sadat, H.; Prax, C. (2002): A meshless formulation for three-dimensional laminar natural convection. *Numerical Heat Transfer*, Part B, Vol. 41, pp. 433-445.

Wang, C.C.; Chen, C.K. (2002): Forced convection in a wavy wall channel. *Int. J. Heat and Mass Transfer*, Vol. 45, pp. 2587-2595.

WU XueHong, SHEN ShengPing, TAO WenQuan. (2007): Meshless Local Petrov-Galerkin CollocationMethod for Two-dimensional Heat Conduction Problems. *CMES: Computer Modeling in Engineering & Sciences.* Vol. 22, no. 1, pp. 65-76.

Xue-Hong, W.; Wen-Quan, T. (2008): Meshless method based on the local weak-forms for steady-state heat conduction problems. *In. J. of Heat and Mass Transfer*, Vol. 51, pp. 3103-3112.

Zhu, T.; Atluri, S.N. (1998): A Modified Collocation & Penalty Formulation for Enforcing the Essential Boundary Conditions in the Element Free Galerkin Method, *Computational Mechanics*, Vol. 21, No. 3, pp. 211-222.

Zhu, T.; Zhang, J.D.; Atluri, S.N. (1998): Local boundary integral equation

(LBIE) for solving nonlinear problems. *Comput. Mech.*, Vol.22, pp. 174-186.